

Dynamic Compressibility, Shear Strength, and Fracture Behavior of Ceramic Microstructures Predicted From Mesoscale Models

by John D. Clayton, R. Brian Leavy, and Reuben H. Kraft

ARL-RP-365

April 2012

A reprint from the AIP Conference Proceedings 1426, 2012, pp. 1039–1044.

NOTICES

Disclaimers

The findings in this report are not to be construed as an official Department of the Army position unless so designated by other authorized documents.

Citation of manufacturer's or trade names does not constitute an official endorsement or approval of the use thereof.

Destroy this report when it is no longer needed. Do not return it to the originator.

Army Research Laboratory

Aberdeen Proving Ground, MD 21005-5069

ARL-RP-365**April 2012**

Dynamic Compressibility, Shear Strength, and Fracture Behavior of Ceramic Microstructures Predicted From Mesoscale Models

John D. Clayton, R. Brian Leavy, and Reuben H. Kraft
Weapons and Materials Research Directorate, ARL

A reprint from the *AIP Conference Proceedings 1426*, 2012, pp. 1039–1044.

REPORT DOCUMENTATION PAGE				Form Approved OMB No. 0704-0188	
<p>Public reporting burden for this collection of information is estimated to average 1 hour per response, including the time for reviewing instructions, searching existing data sources, gathering and maintaining the data needed, and completing and reviewing the collection information. Send comments regarding this burden estimate or any other aspect of this collection of information, including suggestions for reducing the burden, to Department of Defense, Washington Headquarters Services, Directorate for Information Operations and Reports (0704-0188), 1215 Jefferson Davis Highway, Suite 1204, Arlington, VA 22202-4302. Respondents should be aware that notwithstanding any other provision of law, no person shall be subject to any penalty for failing to comply with a collection of information if it does not display a currently valid OMB control number.</p> <p>PLEASE DO NOT RETURN YOUR FORM TO THE ABOVE ADDRESS.</p>					
1. REPORT DATE (DD-MM-YYYY)		2. REPORT TYPE		3. DATES COVERED (From - To)	
April 2012		Reprint		October 2010–February 2012	
4. TITLE AND SUBTITLE Dynamic Compressibility, Shear Strength, and Fracture Behavior of Ceramic Microstructures Predicted From Mesoscale Models				5a. CONTRACT NUMBER	
				5b. GRANT NUMBER	
				5c. PROGRAM ELEMENT NUMBER	
6. AUTHOR(S) John D. Clayton, R. Brian Leavy, and Reuben H. Kraft				5d. PROJECT NUMBER	
				AH80	
				5e. TASK NUMBER	
7. PERFORMING ORGANIZATION NAME(S) AND ADDRESS(ES) U.S. Army Research Laboratory ATTN: RDRL-WMP-B Aberdeen Proving Ground, MD 21005-5069				5f. WORK UNIT NUMBER	
				8. PERFORMING ORGANIZATION REPORT NUMBER	
				ARL-RP-365	
9. SPONSORING/MONITORING AGENCY NAME(S) AND ADDRESS(ES)				10. SPONSOR/MONITOR'S ACRONYM(S)	
				11. SPONSOR/MONITOR'S REPORT NUMBER(S)	
12. DISTRIBUTION/AVAILABILITY STATEMENT Approved for public release; distribution is unlimited.					
13. SUPPLEMENTARY NOTES A reprint from the <i>AIP Conference Proceedings</i> 1426, 2012, pp. 1039–1044.					
14. ABSTRACT Fundamental understanding of dynamic behavior of polycrystalline ceramics is advanced through constitutive theory development and computational modeling. At the mesoscale, microstructures of silicon carbide grains (hexagonal crystal structure) or aluminum oxynitride grains (cubic crystal structure) are subjected to compression or shear at high rates with varying confining pressure. Each grain is resolved by numerous three-dimensional finite elements, and behavior of each grain is modeled using nonlinear anisotropic elasticity. Cohesive fracture models and post-fracture contact are included. Normal and Weibull failure statistics from many simulations are collected and analyzed. Results demonstrate effects of load directionality, confinement, dilatation, elastic anisotropy and elastic nonlinearity, and grain boundary fracture properties on macroscopic (average) failure stresses for loading conditions in the ballistic regime. Predictions demonstrate reasonable agreement with data from macroscopic plate impact, unconfined compression, and flexure experiments.					
15. SUBJECT TERMS ceramics, mesoscale, elasticity, fracture, shock physics, SiC, AlON, shock compression, silicon carbide, aluminum oxynitride					
16. SECURITY CLASSIFICATION OF:			17. LIMITATION OF ABSTRACT	18. NUMBER OF PAGES	19a. NAME OF RESPONSIBLE PERSON
a. REPORT	b. ABSTRACT	c. THIS PAGE			John D. Clayton
Unclassified	Unclassified	Unclassified	UU	12	19b. TELEPHONE NUMBER (Include area code)
					410-278-6146

DYNAMIC COMPRESSIBILITY, SHEAR STRENGTH, AND FRACTURE BEHAVIOR OF CERAMIC MICROSTRUCTURES PREDICTED FROM MESOSCALE MODELS

John D. Clayton¹, R. Brian Leavy¹, and Reuben H. Kraft¹

¹RDRL-WMP-B, U.S. Army Research Laboratory, Aberdeen Proving Ground, MD 21005-5066

Abstract. Fundamental understanding of dynamic behavior of polycrystalline ceramics is advanced through constitutive theory development and computational modeling. At the mesoscale, microstructures of silicon carbide grains (hexagonal crystal structure) or aluminum oxynitride grains (cubic crystal structure) are subjected to compression or shear at high rates with varying confining pressure. Each grain is resolved by numerous three-dimensional finite elements, and behavior of each grain is modeled using nonlinear anisotropic elasticity. Cohesive fracture models and post-fracture contact are included. Normal and Weibull failure statistics from many simulations are collected and analyzed. Results demonstrate effects of load directionality, confinement, dilatation, elastic anisotropy and elastic nonlinearity, and grain boundary fracture properties on macroscopic (average) failure stresses for loading conditions in the ballistic regime. Predictions demonstrate reasonable agreement with data from macroscopic plate impact, unconfined compression, and flexure experiments.

Keywords: mesoscale, ceramics, silicon carbide, aluminum oxynitride, shock compression, fracture.

PACS: 62.20.-x, 62.20.D-, 62.20.-mj, 81.05.Je.

INTRODUCTION

Dynamic deformation and failure behaviors of high-strength ceramics are of interest for military and industrial applications. Properties of importance in the ballistic loading regime include hardness, elastic stiffness, fracture toughness, unconfined compressive strength, dynamic shear strength, and failure probabilities [1-6]. The present work investigates two ceramic materials: silicon carbide (SiC) and aluminum oxynitride (AlON). Mesoscale models are used, wherein each grain in a polycrystalline aggregate is resolved explicitly in a numerical simulation.

This paper is organized as follows. First, models for single crystals and interfacial fracture are listed. Next, three-dimensional microstructures depicted using finite elements are described. Results of simulations considering uniaxial strain

compression, uniaxial stress compression, and shear boundary conditions are reported. Finally, statistics of dynamic failure are analyzed.

THEORY

Essential aspects of the constitutive theory are given here; a comprehensive description will be published later [7]. Consider hyperelastic behavior of single crystals [8-10] within a given polycrystal. Spatial and material coordinates are related by

$$x^a = x^a(X^A, t), \quad (1)$$

where t denotes time. The deformation gradient is

$$F_{\cdot A}^a = \partial x^a / \partial X^A. \quad (2)$$

The symmetric Lagrangian elastic strain is

$$E_{AB} = \frac{1}{2}(F_{\cdot A}^a F_{aB} - G_{AB}), \quad (3)$$

with G_{AB} the covariant referential metric tensor.

Assuming isentropic behavior, internal energy density per unit reference volume U is, to third order in strain,

$$U = \frac{1}{2} C^{ABCD} E_{AB} E_{CD} + \frac{1}{6} C^{ABCDEF} E_{AB} E_{CD} E_{EF}. \quad (4)$$

In Voigt's notation, second- and third-order elastic constants $C^{ABCD} \leftrightarrow C_{\alpha\beta}$ and $C^{ABCDEF} \leftrightarrow C_{\alpha\beta\chi}$.

The first Piola-Kirchhoff stress is

$$\begin{aligned} P^{aA} &= J F^{-1A} \sigma^{ab} = \partial U / \partial F_{aA} \\ &= F_{aB}^a (C^{ABCD} E_{CD} + \frac{1}{2} C^{ABCDEF} E_{CD} E_{EF}), \end{aligned} \quad (5)$$

where $J = \rho_0 / \rho$ is the Jacobian determinant of (2) and σ^{ab} is the Cauchy stress. In the absence of measurements of third-order elastic constants, pressure derivatives of second-order coefficients provide the following approximation [11, 12]:

$$\begin{aligned} C^{ABCDEF} &\approx -\frac{B}{3} \left(\frac{d}{dp} C^{ABCD} G^{EF} + \frac{d}{dp} C^{CDEF} G^{AB} \right. \\ &\quad \left. + \frac{d}{dp} C^{EFAB} G^{CD} \right), \end{aligned} \quad (6)$$

where $p = -\frac{1}{3} \sigma_{aa}^a$ is the Cauchy pressure and

$$B = -J(dp/dJ) = \rho(dp/d\rho) \quad (7)$$

is the bulk modulus, in (6) measured at $J = 1$. Properties for SiC and AlON single crystals are listed in Table 1 [11-15].

TABLE 1. Elastic properties for SiC and AlON crystals.

Property ^a	Value (SiC) ^b	Value (AlON) ^c
C_{11}	5.01	3.01
C_{12}	1.12	1.55
C_{44}	1.61	1.74
C_{13}	0.52	(= C_{12})
C_{33}	5.49	(= C_{11})
C_{111}	-8.44	-10.39
C_{112}	-8.73	-7.13
C_{113}	-8.73	-7.13
C_{123}	-8.88	-5.50
C_{133}	-8.73	-7.13
C_{144}	0.15	-0.81
C_{155}	0.15	-0.81
C_{222}	-8.44	-10.39
C_{333}	-8.44	-10.39
C_{344}	0.15	-0.81
Bulk modulus B	2.22	2.04
Shear modulus G	1.94	1.34
Poisson's ratio ν	0.16	0.23
Density ρ_0 [g/cm ³]	3.227	3.714

^aElastic constants $C_{\alpha\beta}$ and $C_{\alpha\beta\chi}$ in units of Mbar;

Eq. (6) used for $C_{\alpha\beta\chi}$.

^bReferences [11, 13]. ^cReferences [12, 14, 15].

A cohesive zone model addresses intergranular fracture, i.e., stress-induced separation between grains in a given polycrystal [14, 16-20]. Each grain in a polycrystal is treated as a distinct solid body interacting via contact with surrounding grains [21]. Prior to attainment of critical traction t_c , contact between grains is rigid (i.e., perfect bonding). When stresses are sufficient such that the critical traction is achieved at a given interface, separation ensues, with traction held at the critical level until complete separation occurs beyond distance δ_c . Analogous relationships and identical material properties are used for mode I (normal) and mode II (tangential) fracture. Bulk elastic and surface properties are related by [17, 20]

$$t_c \delta_c = K^2 (1 - \nu^2) / E = 2\Gamma, \quad (8)$$

where K is the fracture toughness, $E = 2G(1 + \nu)$ is Young's modulus, and Γ is surface energy. After complete separation occurs in either normal or tangential fracture, atomic bonds are considered irreversibly broken, and boundary facets interact subsequently via locally frictionless contact with material interpenetration prohibited [21]. Fracture properties are listed in Table 2 [22, 23].

TABLE 2. Fracture properties for SiC and AlON.

Property	Value (SiC) ^a	Value (AlON) ^b
t_c [GPa]	0.570	0.306
δ_c [μ m]	0.10	0.06
Γ [J/m ²]	28.1	9.0
K [MPa m ^{1/2}]	5.1	2.5

^aReferences [6, 22].

^bReference [23].

MICROSTRUCTURES

In the absence of microstructures from actual test specimens, finite element meshes of synthetic microstructures are used. Polyhedral grain geometries are produced using a Monte Carlo grain growth algorithm [24]. Volume meshes of tetrahedral elements are created from stereo-lithographic (STL) files of surface representations of grains comprising a given polycrystal [20].

TABLE 3. Features of polycrystalline microstructures.

Feature	Microstructure I	Microstructure II
Dimensions	1×1×1 mm ³	1×1×1 mm ³
No. grains	50	126
Grain size	270 μ m	200 μ m
No. elements	1.59×10 ⁶	1.13×10 ⁶

Two microstructures are considered, with features listed in Table 3. Material properties of SiC or AlON are assigned to either microstructure in a given simulation. In this way, effects of elastic and fracture properties on the overall response are studied while keeping the microstructure (i.e., mesoscale geometry) fixed. Loading in different directions provides an indication of effects of grain structure on anisotropy. Furthermore, different sets of random initial lattice orientations are assigned to polycrystals among different simulations, enabling quantification of effects of anisotropic elasticity.

NUMERICAL SIMULATIONS

Lagrangian finite element calculations are performed using the SIERRA explicit dynamics code [21]. Considered first are results for uniaxial strain compression. A uniform velocity gradient is assigned as an initial condition. The applied strain rate is $\dot{\epsilon} = 10^5/\text{s}$. Under these conditions, the current volume V of the specimen is related to its initial volume V_0 via

$$V = V_0(1 - \dot{\epsilon}t). \quad (9)$$

Figure 1 shows axial stress in a SiC specimen at 6% compression.

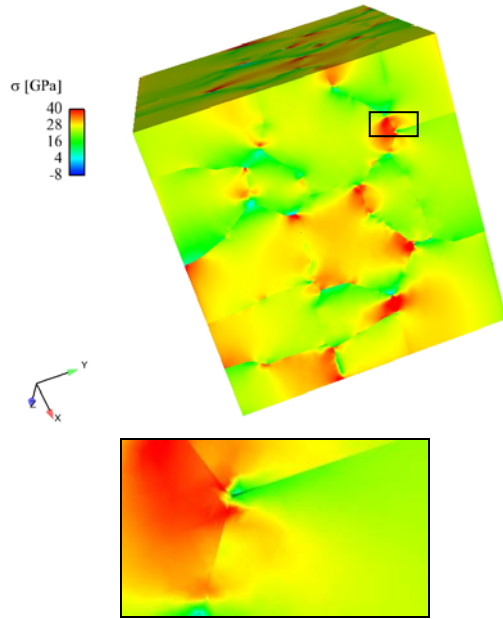


Figure 1. Axial Cauchy stress (positive in compression), microstructure I, SiC, uniaxial strain, $V/V_0 = 0.94$.

In uniaxial strain simulations, one face of the microstructure is assigned a constant velocity in the compression direction while lateral faces are restricted from expanding or contracting. Evident are stress concentrations near grain boundaries and axial splitting cracks typical of brittle materials with low Poisson's ratio [25]. Figure 2 shows average axial stress Σ computed for representative simulations with nonlinear or linear elasticity as

$$\Sigma = \frac{1}{A} \left| \int t^{(n)} dA \right|, \quad (10)$$

where $t^{(n)}$ is the component of traction normal to the compressed face of the microstructure with area A . Also shown for comparison are experimental plate impact data [26-29]. Linear elasticity gives smaller normal stress than corresponding nonlinear models. Figure 3 shows average shear stress

$$\tau = \frac{1}{2} |\Sigma_1 - \Sigma_3|, \quad (11)$$

with $\{\Sigma_1, \Sigma_3\}$ the {maximum, minimum} principle stresses computed similarly to (10). Predictions for SiC are generally lower than experiment; those for AlON are generally closer to experimental data.

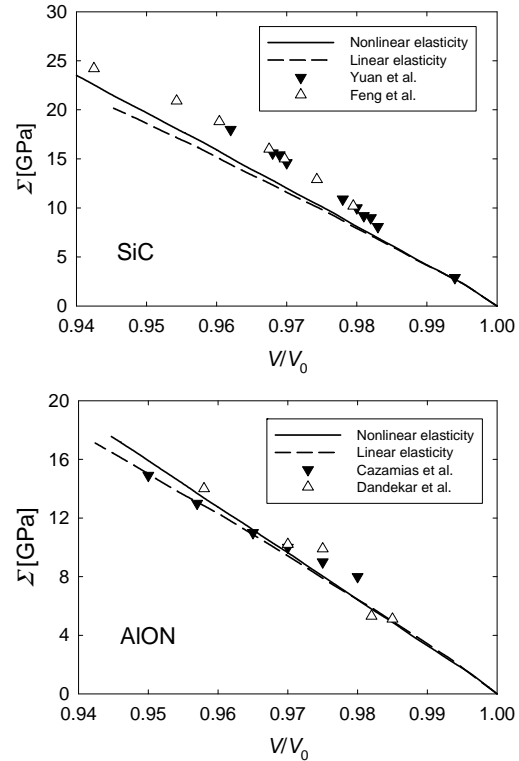


Figure 2. Average axial stress, uniaxial strain.

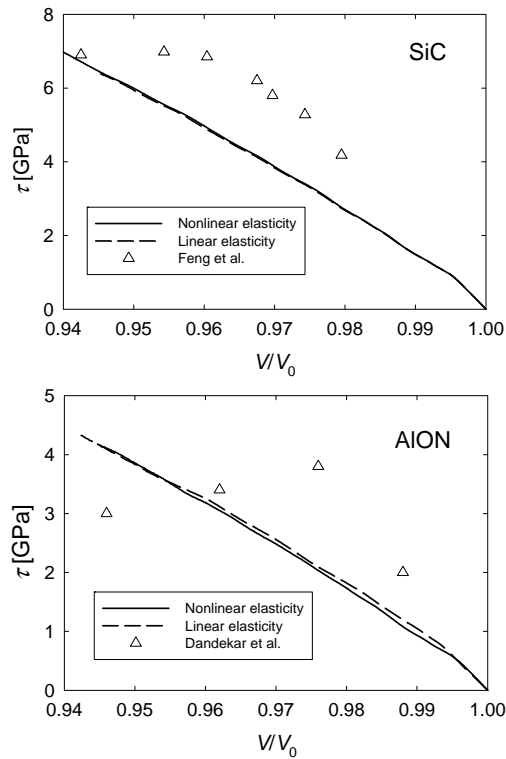


Figure 3. Average shear stress, uniaxial strain.

Unconfined compression simulations are also performed on SiC and AlON microstructures, with initial lattice orientation distributions and loading axes varied among simulations. These and all subsequent results incorporate nonlinear elasticity. Boundary conditions again correspond to a strain rate of $\dot{\epsilon} = 10^5/s$, with a uniform initial velocity gradient prescribed. Peak compressive stresses Σ_x , computed as in (10), are compared with Kolsky bar data [30-32] in Table 4. Again, predictions for AlON are closer to experimental data; however, loading rates in experiments ($\sim 10^3/s$) are smaller than those applied in the numerical simulations.

TABLE 4. Unconfined compressive strength Σ_x [GPa].

	SiC	AlON
Model	4.2-4.9	3.1-3.8
Experiment	5.0-8.2 ^a	3.0-4.0 ^b

^aReferences [30, 31].

^bReference [32].

Shear simulations are also performed on SiC and AlON microstructures, with initial lattice orientation distributions and loading planes and directions varied among simulations. Boundary

conditions provide a shear strain rate of $\dot{\gamma} = 10^5/s$, with a uniform initial velocity gradient prescribed. In some simulations, all faces are free to expand laterally to accommodate dilatation; in others, the face on which the shear traction is applied is prohibited from expanding, thereby increasing the confining pressure that resists dilatation and impedes shear [2-4]. The former conditions are labeled “free”; the latter are labeled “confined.” Figure 4 shows the shear stress component conjugate to the applied strain rate component in representative simulations. Local shear stresses are higher for confined boundary conditions; similar trends are observed for average shear stresses.

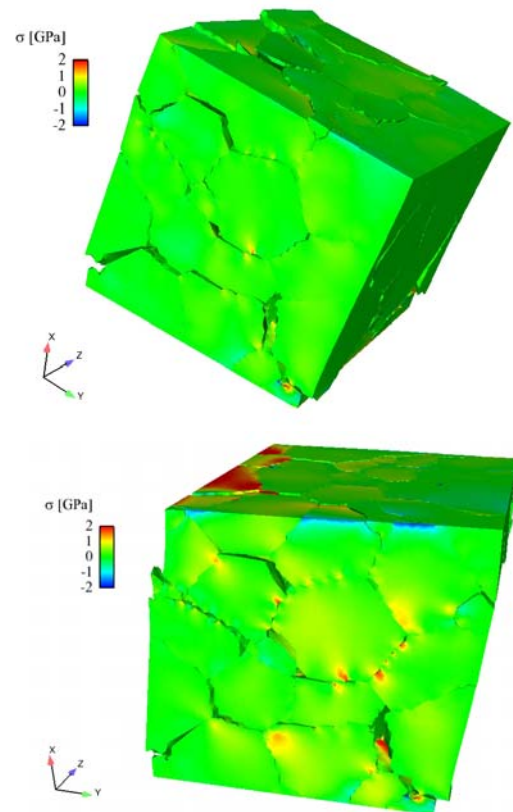


Figure 4. Shear stress, microstructure II, AlON, $\gamma = 0.03$, displacements magnified 5x: unconfined shear loading (upper image), confined shear loading (lower).

Failure statistics from numerous unconfined shear simulations (24 for SiC; 19 for AlON) are now analyzed. Average shear stress τ is computed analogously to (10) for a given polycrystal:

$$\tau = \frac{1}{A} \left| \int t^{(t)} dA \right|, \quad (12)$$

where $t^{(t)}$ is the tangential component of traction applied along A . Shear strength is the (peak) value of τ at which $\partial\tau/\partial\gamma=0$. Table 5 shows normal (i.e., standard Gaussian) statistics computed from discrete values of τ predicted for each material from simulations. The mean value of τ is denoted by $\bar{\tau}$, standard deviation (square root of the variance) by S . Mean strength is lower in AION than SiC, presumably a result of its lower cohesive strength, surface energy, and elastic stiffness. Standard deviation is larger in AION than SiC, possibly a result of greater anisotropy and smaller fracture strength and energy that render AION more sensitive to cracking at grain boundaries or triple junctions favorably oriented for fracture.

TABLE 5. Normal statistics: unconfined shear strength.

Model	SiC		AION	
	$\bar{\tau}$ [GPa]	S [GPa]	$\bar{\tau}$ [GPa]	S [GPa]
Model	0.511	0.013	0.333	0.027

Table 6 lists Weibull statistics for values of τ predicted from simulations; shown for comparison are statistics from static flexure experiments on much larger specimens [5, 34]. A cumulative Weibull distribution predicts probability f of failure at or below a given shear stress τ as

$$f(\tau) = 1 - \exp[-(\tau/\tau_0)^m], \quad (13)$$

with nominal strength τ_0 and Weibull modulus m . Larger m corresponds to lower variability. Weibull parameters are computed from discrete data points by linear fitting to $\ln\{\ln[1/(1-f)]\}$ versus $\ln\tau$, e.g., following [33]. Predictions for SiC exhibit lower variability and greater nominal strength than those for AION, in qualitative agreement with experiments. However, because the mesoscale models do not incorporate initial flaws or spatially variable fracture properties, the present results may under-predict variability.

TABLE 6. Weibull statistics: unconfined shear strength.

	SiC		AION	
	τ_0 [GPa]	m	τ_0 [GPa]	m
Model	0.52	45.2	0.35	14.9
Experiment	0.37-	4.9-	0.29-	2.9-
	0.62 ^a	26.6 ^a	0.81 ^b	26.3 ^b

^aReference [5] ^bReference [34]

CONCLUSIONS

Mesoscale models incorporating nonlinear anisotropic elasticity and cohesive fracture have been used to study dynamic compression and shear of SiC and AION ceramics. Average stresses predicted for compression are in reasonable agreement with experiments on much larger samples of material; agreement between model and experiment is generally closer for AION than SiC. Predictions for dynamic unconfined shear strength demonstrate greater variability for AION than SiC, in qualitative agreement with experimental static fracture statistics.

ACKNOWLEDGEMENT

Prof. A.D. Rollett's research group (Carnegie Mellon University) is acknowledged for providing STL files of polycrystalline microstructures.

REFERENCES

1. Sternberg, J., "Material properties determining the resistance of ceramics to high velocity penetration," *J. Appl. Phys.* **65**, pp 3417-3424 (1989).
2. Shockey, D. A., et al., "Failure phenomenology of confined ceramic targets and impacting rods," *Int. J. Impact Eng.* **9**, pp 263-275 (1990).
3. Curran, D. R., Seaman, L., Cooper, T. and Shockey, D. A., "Micromechanical model for comminution and granular flow of brittle material under high strain rate application to penetration of ceramic targets," *Int. J. Impact Eng.* **13**, pp 53-83 (1993).
4. Gailly, B. A and Espinosa, H. D., "Modelling of failure mode transition in ballistic penetration with a continuum model describing microcracking and flow of pulverized media," *Int. J. Numer. Meth. Eng.* **54**, pp 365-398 (2002).
5. Ray, D., et al., "Effect of microstructure and mechanical properties on the ballistic performance of SiC-based ceramics," in: *Ceramic Eng. Sci. Proc. II*, Wiley, Hoboken, pp 85-96 (2007).
6. Leavy, R. B., Brannon, R. M. and Strack, O. E., "The use of sphere indentation experiments to characterize ceramic damage models," *Int. J. Appl. Ceram. Tech.* **7**, pp 606-615 (2010).
7. Clayton, J. D., Kraft, R. H. and Leavy, R. B., "Mesoscale modeling of nonlinear elasticity and fracture in ceramic polycrystals under dynamic shear and compression," in preparation.
8. Wallace, D. C., *Thermodynamics of Crystals*, Wiley, New York (1972).

9. Thurston, R. N., "Waves in solids," in: *Handbuch der Physik* via/4, Springer-Verlag, Berlin, pp 109-308 (1974).
10. Clayton, J. D., *Nonlinear Mechanics of Crystals*, Springer, Dordrecht (2011).
11. Clayton, J. D., "Modeling nonlinear electro-mechanical behavior of shocked silicon carbide," *J. Appl. Phys.* **107**, pp 013520 (2010).
12. Clayton, J. D., "A nonlinear thermomechanical model of spinel ceramics applied to aluminum oxynitride (AlON)," *J. Appl. Mech.* **78**, pp 011013 (2011).
13. Kamitani, K., et al., "The elastic constants of silicon carbide: a Brillouin-scattering study of 4H and 6H SiC single crystals," *J. Appl. Phys.* **82**, pp 3152-3154 (1997).
14. Gazonas, G.A., et al., "Multiscale modeling of armor ceramics: focus on AlON," *Proc. 27th Army Science Conf.*, Orlando, FL (2010).
15. Batyrev, I. G., et al., "Atomic structure and elastic properties at high pressure of aluminum oxynitride in cubic phase," in: *APS March Meeting*, Bulletin of the American Physical Society (2011).
16. Clayton, J. D., "Dynamic plasticity and fracture in high density polycrystals: constitutive modeling and numerical simulation," *J. Mech. Phys. Solids* **53**, pp 261-301 (2005).
17. Clayton, J. D., "Modeling dynamic plasticity and spall fracture in high density polycrystalline alloys," *Int. J. Solids Structures* **42**, pp 4613-4640 (2005).
18. Kraft, R. H. and Molinari, J. F., "A statistical investigation of the effects of grain boundary properties on transgranular fracture," *Acta Mater.* **56**, pp 4739-4749 (2008).
19. Foulk, J. W. and Vogler, T. J., "A grain-scale study of spall in brittle materials," *Int. J. Fracture* **163**, pp 225-242 (2010).
20. Kraft, R. H., Batyrev, I., Lee, S., Rollett, A. D. and Rice, B., "Multiscale modeling of armor ceramics," *Ceram. Eng. Sci. Proc. IV*, Wiley, Hoboken, pp 143-158 (2010).
21. Jung, J., *Presto 4.16 User's Guide*, Sandia National Laboratories Tech. Rep. SAND2010-3112, Albuquerque, NM (2010).
22. LaSalvia, J. C., Campbell, J., Swab, J. J. and McCauley, J. W., "Beyond hardness: ceramics and ceramic-based composites for protection," *JOM* **62**, pp 16-23 (2010).
23. Corbin, N. D., "Aluminum oxynitride spinel: a review," *J. Eur. Ceram. Soc.* **5**, pp 143-154 (1989).
24. Rollett, A. D. and Manohar, P., "The Monte Carlo method," in: *Continuum Scale Simulation of Engineering Materials*, Wiley-VCH, Weinheim, Ger., pp 77-114 (2004).
25. Chen, W., Ravichandran, G., "Failure mode transition in ceramics under dynamic multiaxial compression," *Int. J. Fracture* **101**, pp 141-159 (2000).
26. Yuan, G., Feng, R. and Gupta, Y. M., "Compression and shear wave measurements to characterize the shocked state in silicon carbide," *J. Appl. Phys.* **89**, pp 5372-5380 (2001).
27. Feng, R., Raiser, G. F. and Gupta, Y. M., "Material strength and inelastic deformation of silicon carbide under shock wave compression," *J. Appl. Phys.* **83**, pp 79-86 (1989).
28. Cazamias, J. U., Fiske, P. S. and Bless, S. J., "Shock properties of AlON," in: *Fundamental Issues and Applications of Shock-Wave and High-Strain-Rate Phenomena*, Elsevier, New York, pp 181-188 (2001).
29. Dandekar, D. P., Vaughan, B. A. M. and Proud, W. G., "Shear strength of aluminum oxynitride," *AIP Conf. Proc.* **955**, pp 505-508 (2007).
30. Pickup, I. M. and Barker, A. K., "Damage kinetics in silicon carbide," *AIP Conf. Proc.* **429**, pp 513-516 (1997).
31. Wang, H. and Ramesh, K. T., "Dynamic strength and fragmentation of hot-pressed silicon carbide under uniaxial compression," *Acta Mater.* **52**, pp 355-367 (2004).
32. Paliwal, B., Ramesh, K. T., McCauley, J. W. and Chen, M., "Dynamic compressive failure of AlON under controlled planar confinement," *J. Amer. Ceram. Soc.* **91**, pp 3619-3629 (2008).
33. Furnish, M. D., et al., "Statistics of the Hugoniot elastic limit from line VISAR," *AIP Conf. Proc.* **955**, pp 521-524 (2007).
34. Warner, C.T., Hartnett, T.M., Fisher, D., Sunne, W., "Characterization of AlON optical ceramic," *Proc. SPIE* **5786**, Orlando, FL, pp 95-111 (2005).

NO. OF
COPIES ORGANIZATION

1 DEFENSE TECHNICAL
(PDF INFORMATION CTR
only) DTIC OCA
8725 JOHN J KINGMAN RD
STE 0944
FORT BELVOIR VA 22060-6218

1 DIRECTOR
US ARMY RESEARCH LAB
IMNE ALC HRR
2800 POWDER MILL RD
ADELPHI MD 20783-1197

1 DIRECTOR
US ARMY RESEARCH LAB
RDRL CIO LL
2800 POWDER MILL RD
ADELPHI MD 20783-1197

1 DIRECTOR
US ARMY RESEARCH LAB
RDRL D
2800 POWDER MILL RD
ADELPHI MD 20783-1197

NO. OF
COPIES ORGANIZATION

ABERDEEN PROVING GROUND

40 DIR USARL
RDRL CIH C
P CHUNG
D GROVE
J KNAP
RDRL WM
J MCCAULEY
RDRL WML B
I BATYREV
B RICE
D TAYLOR
N WEINGARTEN
RDRL WML H
B SCHUSTER
RDRL WMM B
G GAZONAS
RDRL WMP
S SCHOENFELD
RDRL WMP B
C HOPPEL
R KRAFT
D POWELL
S SATAPATHY
M SCHEIDLER
T WEERASOORIYA
RDRL WMP C
R BECKER
S BILYK
T BJERKE
D CASEM
J CLAYTON (10 CPS)
D DANDEKAR
M GREENFIELD
J HOUSKAMP
B LEAVY
M RAFTENBERG
S SEGLETES
C WILLIAMS
RDRL WMP E
S BARTUS
RDRL WMP F
N GNIAZDOWSKI